Demonstration of megavoltage and diagnostic x-ray imaging with hydrogenated amorphous silicon arrays

Larry E. Antonuk, John Boudry, Weidong Huang, Daniel L. McShan, Edward J. Morton, and John Yorkston
Department of Radiation Oncology, University of Michigan Medical Center, Ann Arbor, Michigan 48109

Michael J. Longo
Department of Physics, University of Michigan, Ann Arbor, Michigan 48109

Robert A. Street
Xerox Palo Alto Research Center, 3333 Coyote Road, Palo Alto, California 94304

(Received 8 November 1991; accepted for publication 6 August 1992)

Flat-panel imagers consisting of the first large area, self-scanning, pixelated, solid-state arrays made with hydrogenated amorphous silicon (a-Si:H) are under development by the authors for applications in diagnostic x-ray and megavoltage radiotherapy imaging. The arrays, designated by the acronym MASDA for multi-element amorphous silicon detector array, consist of a two-dimensional array of a-Si:H photodiodes and thin-film transistors and are used in conjunction with scintillating materials. Imagers utilizing MASDA arrays offer a variety of advantages over existing technologies. This article presents initial megavoltage and diagnostic-quality x-ray images taken with several such arrays including the first examples of anatomical-phantom images. The external readout electronics and imaging techniques required to obtain such images are outlined, the construction, operation, and advantages of the arrays briefly reviewed, and the future potential of this new technology discussed.

Key words: diagnostic x-ray imaging, megavoltage portal imaging, amorphous silicon, digital imaging, flat-panel imagers

I. INTRODUCTION

The availability of a practical, self-scanning, two-dimensional, solid-state, diagnostic x-ray imaging device has long been recognized as an important and probably necessary stepping-stone toward the goal of clinical implementation of fully digital, photoelectronic radiology.[1,2] Over the last 20 years, there have been tremendous strides in the development of an obvious candidate—charge-coupled device (CCD) imaging arrays which are fabricated from wafers of crystalline silicon (c-Si). However, the technology associated with c-Si fabrication is not appropriate for the production of large area devices, and the largest reported CCDs are only about 5.5×5.5 cm.[3] Consequently, the creation of a large area imager from this technology would entail "tiling" a considerable number of such imaging arrays which would be a rather difficult and expensive process.

Concurrent with these developments, a variety of thin-film semiconductor technologies, including that of hydrogenated amorphous silicon (a-Si:H), have been rapidly emerging. Devices made of a-Si:H, such as photodiodes and field effect transistors (FETs), are produced on a glass, quartz, ceramic, or metal substrate by gas deposition in a reaction vessel.[4] Rapid development of a-Si:H followed the discovery that the addition of hydrogen serves to reduce the density of unpaired valence electrons, or dangling bonds, which create electron and hole traps. This allows a-Si:H to exhibit some of the desirable properties of crystalline solid-state materials.[4] Semiconductor properties are affected by the addition of dopants in the reaction vessel. In an idealized picture of the resulting material, the short-range structure is similar to that of c-Si but the long-range structure is of a more random nature. This change in structure results in electron and hole mobilities for a-Si:H (~ 2 and 10^{-2} cm^2/V-s, respectively) which are considerably less than those for crystalline silicon (~ 1300 and 500 cm^2/V-s, respectively).[5] Moreover, while the mobility of charge carriers in c-Si increases with decreasing temperature, it actually decreases in the case of a-Si:H.[4] A further limitation with present thin-film technologies is that the minimum feature size is currently 2 to 5 μm compared to submicron feature sizes for crystalline devices.

Despite these limitations, the inherent large-area nature of a-Si:H technology has spurred a tremendous effort to create devices of ever greater sophistication. Over the last two decades, a-Si:H photodiodes have been extensively developed for a variety of photovoltaic applications including solar cells, scanners, and copiers. Presently, one of the more prominent technologies to emerge in the world-wide race to develop flat-panel displays involves thin-film transistors made from a-Si:H and related materials. These so-called active-matrix-addressed, thin-film-transistor, liquid crystal displays utilize a plane of such transistors to control the polarization of light in liquid crystal material.[6] Thus far, prototype 14-in. displays containing more than a million a-Si:H transistors have been produced. The current limit to the maximum useful area of devices is about 30×30 cm, and efforts are underway to increase this to 100 cm on the diagonal by 1996.[7]

The possible use of a-Si:H for radiation detection appli-

 0094-2405/92/61455-12$01.20

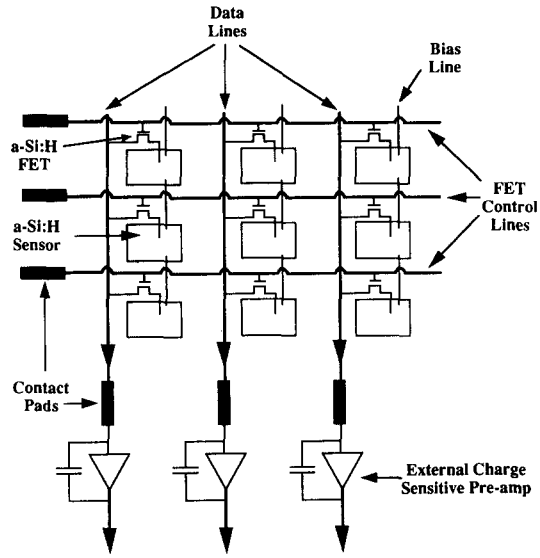

FIG. 1. Schematic diagram of a top view of a corner segment of the array showing the row–column organization of photodiode sensors and FETs, as well as bias, FET control, and DATA lines (not to scale). The FET and DATA lines are shown terminating at contact pads to the left and bottom of the array segment shown. The charge sensitive preamplifiers are external to the arrays.

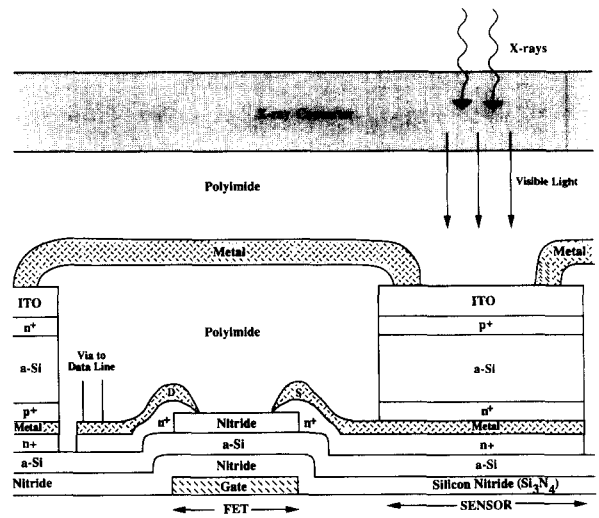

FIG. 2. Detailed diagram of a side profile of the n-i-p sensor and FET for a single pixel (not to scale). The view shows the cross-sectional details of a FET-sensor combination perpendicular to the direction of the FET control lines. The drain contact of the FET leads to a DATA line, not visible in this diagram, by means of a vertical conducting pathway (labeled via). The FET control line is perpendicular to the plane of the diagram and passes through the gate contact of the FET, labeled Gate. The symbols S and D label the source and drain of the FET while nitride represents silicon nitride dielectric. The symbols n^+, p^+, and a-Si:H refer to n doped, p doped, and intrinsic amorphous silicon, respectively. A glass substrate (not shown) forms the mechanical surface upon which these structures are deposited. Incident radiation is sampled indirectly by means of an x-ray converter positioned on top of the array.

cations is being explored by a number of groups. Since 1985, one of the authors (Street) has collaborated with scientists at Lawrence Berkeley Laboratory in examining the possibility of using a-Si:H technology for a wide variety of particle physics and medical applications.[8] Another group is pursuing the development of small panels ($\sim$24 $\times$22 mm) of a-Si:H photodiode sensors deposited on ceramic scintillators for use in x-ray CT.[9] The possibility of creating detectors made up of interleaved a-Si:H and metal layers which are sufficiently thick to allow direct detection of diagnostic quality x-rays has also been reported.[10] Diagnostic x-ray imaging using a linear a-Si:H photodiode scanner array which is optically coupled to a two-dimensional fiber-optic matrix and phosphor screen has also been demonstrated.[11]

II. DESCRIPTION OF THE ARRAYS

Since 1987, our collaboration has been pursuing the development of the first two-dimensional a-Si:H arrays for real-time diagnostic x-ray and megavoltage radiotherapy imaging.[12–15] These arrays consist of a regular arrangement of imaging pixels, each of which is made up of an a-Si:H photodiode sensor coupled to an a-Si:H FET. Figure 1 is a schematic diagram showing the geometric arrangement of the pixels and associated bias, control, and data lines, while Fig. 2 illustrates a profile view of an individual sensor–FET combination. Electronics external to the arrays provide bias and switching voltages to the arrays and convert analog signals from the pixels to digital form.

The photodiode has a doped-intrinsic-doped structure (p-i-n or n-i-p) in which the i-layer constitutes most of the thickness ($\sim$1 μm) compared to the considerably thinner doped layers (10 to 100 nm). Ohmic contacts to the sensor are formed by a layer of chrome underneath the lower doped layer and by a layer of the transparent conducting material, indium tin oxide (ITO), on top of the upper doped layer. A network of metal lines over the arrays contact the ITO layer of each sensor and provide an external reverse bias voltage, V_{bias}, which serves to deplete the intrinsic layer of the photodiode.

The incident radiation signal is sampled indirectly by means of an x-ray converter placed over the array, as shown in Fig. 2. For diagnostic x-ray imaging, this converter can be a phosphor screen or some other suitable material like CsI(Tl). For megavoltage imaging, a metal plate/phosphor screen combination can be used or, alternatively, a thick scintillator, but perhaps with the loss of spatial resolution. The sensors are sufficiently thin that there is negligible signal generated in them through direct interaction of the incident radiation. Thus the sensitivity to radiation is entirely that of the x-ray converter. Such sensitivities have been extensively measured and reported for phosphor screens and CsI(Tl) for diagnostic energies. For megavoltage energies, the sensitivities for metal sheets/phosphor screens and $ZnWO_4$ crystals have recently been reported.[16–18]

During imaging, incident high-energy photons are converted to electrons in the x-ray converter resulting in the generation of light photons. Virtually all photons emitted from the scintillator which enter the photodiodes are absorbed creating an electron-hole pair per absorbed photon. The output signal from the sensor is created by the collec-

tion of the electron-hole pairs liberated in the depleted intrinsic region of the photodiodes. The doped layers provide the rectifying electrical junction which minimizes the leakage current. However, the charge released in these regions does not contribute significantly to the output signal due to the very short minority carrier lifetimes in these layers. On the other hand, the undoped material has few defects (typically 10^{15} cm^{-3}) and can sustain a wide depletion layer and long recombination times. Thus a p-n junction without the undoped layer is an ineffective sensor, and in the n-i-p or p-i-n devices the doped layers are made as thin as possible.

The FETs have a standard structure consisting of source, drain, and gate contacts. The width and length of the FET gate determine the conductivity and switching properties of the transistor.[15] As shown in Fig. 1, there is a common FET control line connected to all the FET gates along each row and a common DATA line connected to all the FET drains down each column. The source contact of each FET is connected to the lower contact of its corresponding photodiode (Fig. 2). Manipulation of the voltage level of the individual FET control lines by the external electronics allows the conductivity of FETs along the corresponding rows to be varied. Polyimide, a nearly transparent plastic material, serves to provide a planarization and passivation layer.

During imaging, with the FETs nonconducting, the electron-hole pairs generated in the depletion layer by incident light photons result in a discharging of the sensor capacitance, which is initially charged to a voltage of $\sim V_{bias}$. The degree of this discharging constitutes the integrated imaging information. During readout, this information is sampled and the corresponding sensors are reinitialized to $\sim V_{bias}$ by rendering the FETs along a single row conducting. This results in a current flow along the DATA lines to the addressed pixels. The resulting current pulses are amplified and integrated by external charge-sensitive preamplifiers, one preamplifier per DATA line. The resulting analog information is then multiplexed and digitized by further external electronics. After a given row is read out, the associated FETs are made nonconducting and the process is repeated for the next row until the entire array has been sampled to give a single image or frame. In this readout scheme, measurement of the pixels also initializes them. This allows images to be acquired in a consecutive fashion. A description of other, more involved, aspects of the dynamic behavior of the pixels may be found elsewhere.[19]

Thus far, two generations of arrays have been made[15,20] and some of their characteristics are summarized in Table I. The first generation of devices had a format of 64 DATA lines by 40 FET control lines for a total of 2560 pixels. Two versions of these arrays were designed with pixel-to-pixel pitches of 270 and 900 μm. While the size of these arrays are small, they have and continue to serve as convenient and relatively inexpensive devices for testing array improvements due to variations in processing steps during array fabrication, for qualifying electronic design, and quantifying basic array properties.[15,19,21] A second generation of arrays whose design has been tailored to megavoltage imaging has recently been completed with 256 DATA lines by 240 FET lines for a total of 61 440 pixels. These arrays have a 450-μm pitch and are the most recent step toward our goal of $\sim$25 cm by 25 cm arrays with a similar pitch for megavoltage imaging. To our knowledge, these 450-μm arrays are the largest self-scanning, solid-state imaging devices ever reported with an active area approximately four times that of the largest CCDs.[3] In the present array designs, it is necessary to avoid overlap of the sensors with the DATA lines, the FET control lines, and the transistors. Such overlap would cause undesirable capacitive effects. As a consequence, the sensors are smaller than allowed by the pixel-to-pixel pitch, as schematically illustrated in Fig. 2. This, plus the fact that the bias lines cover a portion of the sensor, means that the fraction of the array surface that is sensitive to light, called the fill factor, is less than unity. The fill factor for each array is shown in Table I.

TABLE I. Summary of characteristics of arrays thus far built by this collaboration. See text for details.

Array Pitches (μm)	270	900	450
Array format (DATA×FET)	64×40	64×40	256×240
Array dimensions (cm^2)	1.73×1.08	5.76×3.60	11.5×10.8
Fill factor	0.48	0.83	0.62
Total array light efficiency			
$CaWO_4$	21%	36%	27%
CsI(Tl) and Gd_2O_2S:Tb	27%	52%	39%
Maximum theoretical Frame rate (fps)	~760	~40	~110

One important array parameter is the fraction of light emitted by the scintillator and used by the sensor. Figure 3 shows the absolute efficiency of a typical n-i-p a-Si:H sensor with a microcrystalline (μc-Si:H) p-layer. Such sensors are standard in our most recent arrays. The absolute efficiency of n-i-p sensors composed entirely of a-Si:H is typically lower. Superimposed on this sensor data are the spectral emission distributions for three scintillators, $CaWO_4$, CsI(Tl), and Gd_2O_2S:Tb. The product of the sensor effi-

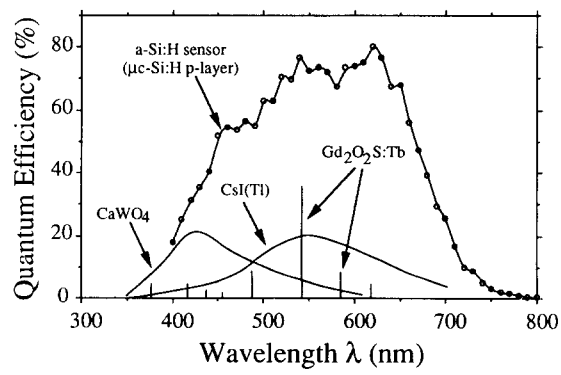

FIG. 3. The absolute light quantum efficiency of an n-i-p sensor with a μc-Si:H p-layer as a function of wavelength. Light output of three common scintillators, in arbitrary units, is superimposed for comparison.

ciency with the spectral distributions is approximately 43%, 63%, and 63% for $CaWO_4$, CsI(Tl), and Gd_2O_2S:Tb, respectively. The product of each of these numbers and the fill factor of an array gives the total detection efficiency of the light emitted from the corresponding scintillator. For each of the three scintillators, and using the sensor data of Fig. 3, the total light detection efficiency for the various arrays is given in Table I. It should be noted that processing variations can alter the sensor efficiencies by up to a total of 5% to 10% so that the values given in Table I are approximately representative.

Another important property of such arrays is the maximum frame rate at which images can be extracted. An absolute upper limit for this quantity is given by the inverse of the product of the time required to reinitialize a row of pixels times the number of rows per array. The reinitialization of a pixel follows an exponential behavior, and a characteristic time constant can be measured for pixels for a given array.[22] To reinitialize the pixels to 1 part in 10^3, ~ 7 time constants are required. With this degree of initialization and for a FET-on voltage of $+10$ V, maximum theoretical frame rates for the various arrays based upon measurements of pixel reinitialization times[22] are presented in Table I. While these frame rates are limited only by the pixel time constants, practical considerations such as transient settling times, multiplexing and digitization speeds, and data transfer and image processing rates further restrict the achievable frame rates. Such practical considerations could limit achievable frame rates to approximately one-half of the theoretical rates.

Imagers based upon such arrays will offer a number of definite advantages. As the preamplifiers are the only external electronics that must be in close proximity to the array, it is reasonable to expect that the imager can be packaged so as to have a maximum thickness of ~ 2 cm. This promises an attractively compact alternative to current real-time megavoltage and x-ray image intensifier (XRII) systems which are considerably bulkier. Such compactness could lead to relatively portable imaging devices. The random structure of a-Si:H makes it particularly radiation damage tolerant[23–25] which is important in both diagnostic and megavoltage imaging. In the case of diagnostic fluoroscopy, such flat-panel imagers will eliminate the problems of veiling glare, distortion (both pin-cushion and that due to factors such as stray magnetic fields), vignetting, and other limitations suffered by XRII systems.[15] For megavoltage imaging, the detective quantum efficiency (DQE) and hence image quality offered by flat-panel imagers will be higher than that offered by current camera-fluoroscopy imagers, both those employing mirrors and fiber-optic reducers. This is because present camera-fluoroscopy imagers have low light efficiency ($\sim 0.05\%$) and are light quantum limited[16,26] while the comparatively higher light efficiency of the flat-panel imagers (Table I) allows them to be input quantum limited. These imagers offer fast, inherently digital readout, and the array surface can be configured to the geometric shape which best matches the application. Furthermore, dynamic ranges from individual pixels as large as ~ 1300 to 1, limited by noise in the external electronics, have been obtained from these arrays, and it is anticipated that much higher values may be attainable. As these imagers can use the same scintillating materials as those used in current radiographic, fluoroscopic, and megavoltage imagers, the sensitivity to radiation will be about the same, although dual-screen radiography will retain a sensitivity advantage.

III. EXPERIMENTAL DESCRIPTION

Images were acquired with arrays of 270-, 450-, and 900-μm pitch. All the arrays had an n-i-p sensor structure with a 50-nm n-layer and an ~ 1-μm i-layer. The p-layer thicknesses for the arrays were 100, 50, and 20 nm, respectively. In addition, the p-layer of the 900-μm array was made of microcrystalline silicon (μc-Si:H) rather than a-Si:H. The arrays were fabricated at Xerox, PARC on Corning 7059 glass substrates. For the 270-μm array, $\sim 98.8\%$ of the pixels were operational and were previously determined to offer a uniformity of response better than 1%.[21] For the 900-μm array, some or all of the pixels along 3 DATA lines on the periphery were nonfunctional, possibly due to a break in the DATA line. Only five pixels were nonoperational on other parts of this array. Two 450-μm arrays were used. For each of these arrays, a total of ~ 18 DATA lines had to be isolated from the external electronics. This was due to large negative signals from these lines which caused saturation in the external electronics. These anomalous signals are due to the failure of a single transistor somewhere along each affected DATA line. Such failed transistors can be isolated by laser ablation techniques thereby restoring the utility of the rest of the pixels along the affected DATA line. While this has been recently demonstrated,[27] technical considerations have thus far made it impracticable to use such repaired arrays with the electronics described in this article. Apart from these problem DATA lines, $\sim 1\%$ to 2% of the pixels on the 450-μm arrays were nonfunctional. Each array is mounted on a printed circuit board (the "motherboard") whose traces are connected to the contact pads of the FET control and DATA lines on the substrate. Electrical connection between the array and the motherboard was made using either elastomeric connectors or wire bonding. The purpose of the motherboard is to act as an intermediate stage for electrical connection to external electronics, as well as to provide mechanical support for the array.

The electronic readout system, constructed at Michigan, is illustrated in Fig. 4. A circuit (the "FET switcher") incorporating 32-channel digital shift registers paired with display driver outputs (Supertex HV5708PJ) was used to vary the voltages of the FET control lines under computer control via a Jorway model 41 output register. As the signals from the pixels are relatively small (on the order of ~ 10 to 400 pC), preamplification of these signals close to the array is necessary before transferring the signals to an ADC for digitization. Furthermore, the presence of 64 and 256 independent DATA channels on the 40×64 and 240×256 pixel arrays, respectively, makes it advantageous to perform some multiplexing of the pixel signals in order to avoid the necessity of requiring one ADC per DATA chan-

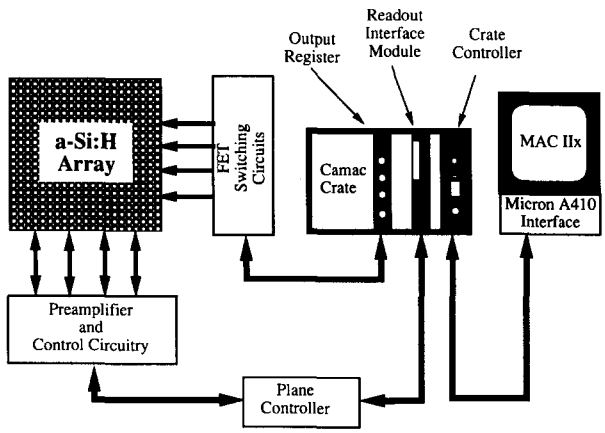

FIG. 4. Block diagram illustrating the various components in the readout system used to acquire images from the array.

nel. In the current version of the electronics, this preamplification and multiplexing is performed by means of circuitry incorporating the RAL-103 charge multiplexing chip designed by Rutherford–Appleton Laboratory for wire-chamber readout in particle physics applications.[28] Each chip has 16 inputs and a single output so that, with further stages of multiplexing, either one or two ADCs were sufficient. Analog signal information was sent to a pair of modules containing a 12-bit voltage sensitive ADC and buffer memory (the "plane controller") and an interface to a CAMAC crate, respectively. These modules were originally designed as part of a system for proportional chamber readout in particle physics research.[29] The host computer was a Macintosh IIx, and data was transferred between the CAMAC crate and the computer by means of a CAMAC crate controller (type 392 MAC-CC crate controller) and a Macintosh NuBus card (A410 Micron interface), both specifically designed at CERN to allow data transfers (up to 500 kbytes/s) through memory-mapped instructions.[30]

For megavoltage imaging, an $\sim$1-mm-thick sheet of copper bonded to a Cronex Lightning-Plus screen (86.8 mg/cm^2 of calcium tungstate, $CaWO_4$) was placed over the arrays. For diagnostic x-ray imaging, a Kodak Lanex Fast B screen (133 mg/cm^2 of gadolinium oxysulfide, Gd_2O_2S:Tb) was used. The significantly different signal sizes generated in a-Si:H sensors by these two screens for megavoltage and diagnostic energies has previously been studied.[13,22] The selection of these screens for the two imaging situations is governed by the desirability of utilizing a substantial fraction of the signal capacity, and hence dynamic range, of the pixels without saturating them. Megavoltage images were acquired with a Varian Clinac 1800 accelerator which provided 130 ± 1 pulses/s of $\sim$5-μs width. Diagnostic x-ray images were acquired with an Oldelft Simulix Y simulator with a GE Maxiray 100 tube source operated in fluoroscopic mode.

The array operating conditions were as follows: a FET-off voltage of -5.0 V, a FET-on voltage of 10.0 V, and a sensor bias, V_{bias}, of -5.0, -2.5, and -2.0 V for the 270- , 450- , and 900-μm arrays, respectively. Under such conditions, the sensors and FETs exhibit leakage currents of $\sim$0.1 pA/mm^2 and $\sim$0.01 pA, respectively. Images were acquired in consecutive fashion, one frame after another with an uninterrupted radiation signal. For diagnostic imaging, the electronics were adjusted to read out the entire array at a rate of one frame every 3, 2, and 1 s for the 270- , 450- , and 900-μm arrays, respectively. For megavoltage imaging, a prescaler was used to count pulses from the accelerator and to issue a trigger to the readout electronics every "n" pulses. Following this trigger, a single row of pixels would be read out before the arrival of the next pulse from the accelerator. Furthermore, the timing was adjusted so that the readout of the pixels began only after the light from the $CaWO_4$ screen, lasting $\sim$30 μs, had completely decayed. In this fashion, each row of pixels was guaranteed to integrate the signal information from the same number of beam pulses.

During the integration period between successive reads of a pixel, the initial bias across each photodiode, $\sim V_{bias}$, reduces due to integration of both the light-induced signal and the difference in leakage current from the photodiode and FET.[19] Consequently, even under conditions of zero illumination there is an "offset" signal due to a combination of the integration of this leakage current difference, a transient arising from the switching of the FET voltage, and an offset from the external electronics.[21] The measured response of a pixel as a function of increasing light (and radiation) therefore exhibits an offset under conditions of no light, followed by an approximately linear increase in response with light, and terminating in a plateau when the pixel saturates due to almost complete discharge of the sensor capacitance.[21,22]

In the present case, we have chosen to parametrize the measured light response function of the pixels by a linear relation:

$$\mathrm{ADC}^{(p)}(L,d,f) = G_0^{(p+\mathrm{el})}(d,f) + [L \times G_1^{(p+\mathrm{el})}(d,f)], \quad (1)$$

where $\mathrm{ADC}^{(p)}$ is the "raw" digital value of the measured signal for the pixel at DATA line d, FET line f, and is a function of the amount of light captured, L. The values of $\mathrm{ADC}^{(p)}$ give the raw or unprocessed image. $G_0^{(p+\mathrm{el})}$ is the constant offset due to pixel and external electronics effects and $G_1^{(p+\mathrm{el})}$ is the gain factor due to the combined effect of pixel and external electronics. The values for G_0 and G_1 were determined for each pixel on the arrays with a calibration procedure involving separately averaging 10 to 100 frames of dark and flood field image data. This data is taken under conditions nearly identical to those used for imaging. For most flood-field measurements, an appropriate amount of solid water was positioned over the array to provide an average signal level approximately the same as for the object to be imaged. The calibration constants, G_0 and G_1, were then used to correct for the pixel-to-pixel and external electronic channel variations by solving for L in Eq. (1) and rescaling the result so as to represent the same number of bits of precision as was generated by the ADC. While the light response of the pixels in fact becomes nonlinear as saturation is approached, this has not yet been

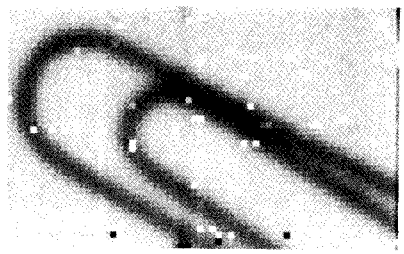

FIG. 5. Diagnostic x-ray image of a paper clip acquired with a 270-μm 64$\times$40 a-Si:H array and taken at 65 kVp with a 30-mAs exposure. The image is the raw data without pixel calibration factors or other image processing. The greyscale for this and all following array and digitized film images is inverted compared to that of conventional x-ray film.

adequately studied to allow a parametrization by a higher order polynomial or some other function. However, in these initial investigations, the maximum pixel signal sizes were chosen to be well below saturation so that the use of a linear form for the parametrization was adequate. A more complete representation of the response function awaits the results of ongoing studies of the behavior of the arrays. This may improve the quality of the images and should extend the useable dynamic range of the arrays. Initial images acquired with these arrays and readout system are reported in the following section.

IV. RESULTS

A. Images with 270-μm array

Figure 5 is a raw a-Si:H x-ray contact image of a paper clip taken at 65 kVp with a 10-mA tube current and a 3-s integration period. For reasons of enhanced presentation, the greyscale chosen for this and all following array and digitized film images has been inverted compared to that of conventional x-ray film. The DATA lines lie vertically in this and all following a-Si:H images [with the exception of Fig. 12(a)]. No corrections have been applied to this image other than to select a window level and width for display, as was done for all the images presented. The salt and pepper noise in the image is due to the variations in offsets and gains among the pixels. The brightest pixels correspond to the $\sim$1.2% of the pixels that were essentially nonfunctional. Figure 6 is the raw image of a Nuclear Associates Type 18 bar phantom rotated $\sim$45° with respect to the array grid with the same conditions as for Fig. 5. From left to right, the patterns correspond to 0.71, 1.0, 1.4, and 2.0 lp/mm. The 1.4 lp/mm pattern is clearly resolvable, and this is consistent with the resolution expected with an array of 270-μm pitch. The intrinsic resolution offered by such arrays is limited by the degree to which cross-talk exists between the pixels. This is currently under investigation.

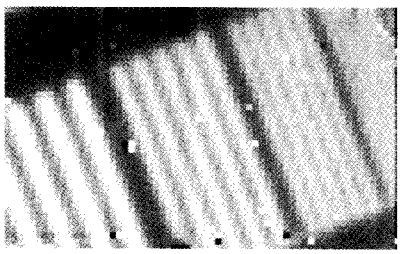

FIG. 6. Diagnostic x-ray image of a bar phantom acquired with the same array and conditions as Fig. 5.

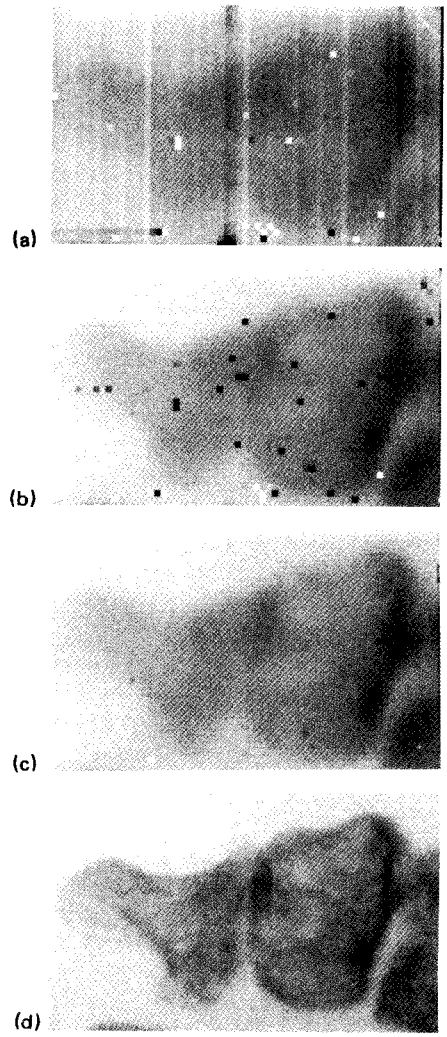

FIG. 7. Diagnostic x-ray images of the 5th toe of a 3M foot phantom. (a) Image acquired with the 270-μm array of Fig. 5 taken at 120 kVp with a 24-mAs exposure. The image is the raw data without pixel calibration factors. (b) Image 7(a) after application of calibration constants for the individual pixels. (c) Image 7(b) after application of a 3$\times$3 median filter to the non-functional pixels. (d) Digitized film image taken at 65 kVp with an 0.35-mAs exposure.

Figure 7 shows x-ray images of the 5th toe of a 3M foot phantom. Figure 7(a) is a raw a-Si:H image taken at 120 kVp with 8 mA and a 3-s integration period. The vertical stripes, which are more visible than in Figs. 4 and 5 due to a smaller window width, are caused by differences in the offsets and gains of the individual external electronic amplifier channels. Figure 7(b) is the same image data as Fig. 7(a) after application of the pixel-by-pixel calibration. The dark spots correspond to poorly functioning, or "bad," pixels. Figure 7(c) is the Fig. 7(b) image data after application of a 3$\times$3 median filter to these bad pixels. This filter replaces the value of the bad pixel with the median of the 9 pixels centered on the bad pixel. This removes the dis-

tracting effects of these bad pixels, and otherwise has little discernible effect upon the image quality. Figure 7(d) is an image taken with Kodak TMG film using a Kodak X-Omatic cassette with a double-sided screen (Lanex Regular) at 65 kVp with a 50 mA, 0.007-s exposure. The film was digitized with a Lumisys Dis-1000 film scanner using a 125-μm sampling interval and spot size. For this and all other film images reported, the geometric conditions under which the image was acquired were identical to those used for the corresponding array image, unless otherwise stated. In Fig. 7(b)–(d), the various anatomical features of the toe including the distal, middle, and the head of the proximal phalanges are clearly visible on the left, middle, and right of the images, respectively. The contrast information content of the digitized film image is largely reproduced in the a-Si:H image. While the first x-ray image (of a very high contrast object) taken with one of these a-Si:H arrays, using completely different electronics based on a readout chip developed for a FAX scanner, was previously reported,[20] the present image of a low-contrast object (fifth toe) is the first such anatomical-phantom image reported with this new technology. (This image and those of Figs. 5 and 6 were first presented on 12 July, 1991 at the World Congress on Medical Physics and Biomedical Engineering held in Kyoto Japan, 7–12 July, 1991.)

The relatively large exposures required to make these 270-μm a-Si:H array images were necessitated by two limitations. First, while the array chosen for this study was well characterized and had very few nonfunctional pixels, its polyimide layer was incorrectly applied. As a consequence, its sensitivity to light was only $\sim$7% that of "normal" arrays.[22] Second, the readout electronics used for these images are specifically intended for megavoltage imaging with the 450- and 900-μm arrays. Thus, in order to handle the large signals associated with that application (up to $\sim$400 pC), the RAL-103 preamplifiers, which can handle up to $\sim$500-pC signals, were chosen. Not surprisingly, the noise characteristics of these chips become poorer as the signal sizes approach a few pC. At the same time, the maximum useable signal sizes from the 270-μm array is only $\sim$20 pC. Consequently, it was necessary to use as much of the signal capacity of the pixels as possible in order to improve the preamplifier performance. Thus, for the purpose of this diagnostic imaging demonstration and constrained by these two limitations, a thick phosphor screen ($\sim$133 mg/cm^2), a relatively long integration period ($\sim$3 s), a large tube current, and a high x-ray energy were employed in order to get as large a signal as practical. Diagnostic images acquired with the other arrays were obtained with more reasonable exposures, as reported below.

B. Images with 900-μm array

Megavoltage and diagnostic x-ray array and film images of the same region of a 3M head phantom are shown in Fig. 8. (The images in Figs. 8 and 13 were first presented on 7 November, 1991 at the Annual Meeting of the American Society for Therapeutic Radiology and Oncology held in Washington, D.C. 4–8 November, 1991.) In all cases, the image is a right lateral (with respect to the radiation source) of the region in the vicinity of the sella turcica. Four marker BBs with $\sim$2-mm diameter were positioned on the surface of the phantom so as to aid in the identification of visible features common to the various images. The midline of the head was positioned 100 cm from the radiation source while both the array and the film cassettes were at 112 cm. Figure 8(a) is an array image acquired with a beam energy of 6 MV, a dose of 3.7 monitor units (MUs), and a 6$\times$6 cm field at isocenter (100 cm) to reduce the scatter. The calibration of the therapy machine is such that 1 MU delivers 1 cGy to tissue at a depth of maximum dose at 100 cm from the radiation source, for a 10$\times$10 cm field. Figure 8(b) is a digitized film image taken at 6 MV with 5 MUs using Kodak TMG film and a Kodak X-Omatic L Radiation Therapy cassette containing an

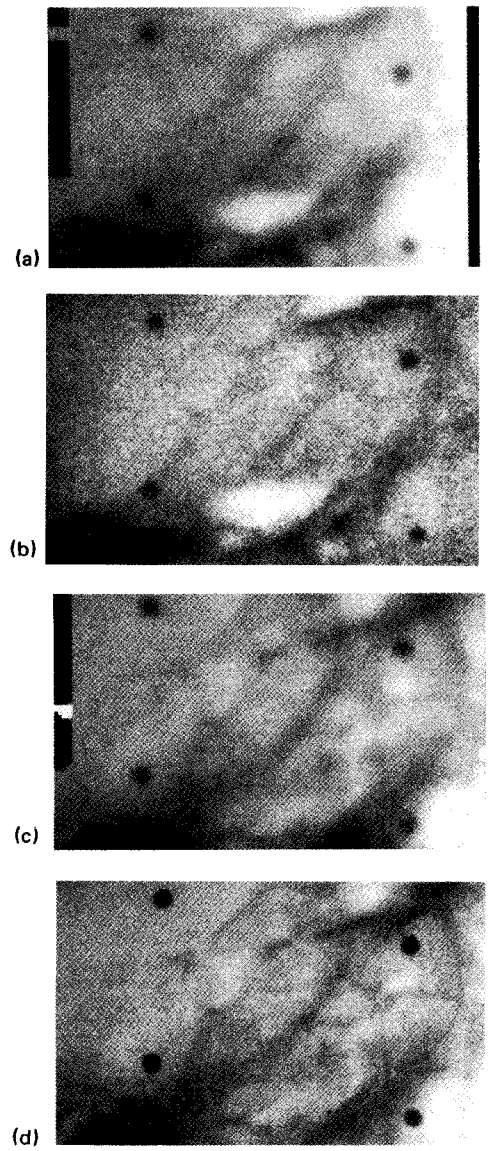

FIG. 8. Megavoltage and diagnostic lateral x-ray images of the sella turcica region of a 3M head phantom. (a) Megavoltage image acquired with a 900-μm array taken at 6 MV with 3.7 MUs. (b) Digitized megavoltage film image taken at 6 MV with 5 MUs. (c) Diagnostic x-ray image acquired with the 900-μm array in the same region as for Fig. 8(a) and taken at 75 kVp with a 7.0-mAs exposure. (d) Digitized diagnostic film image taken at 74 kVp with a 3.0-mAs exposure.

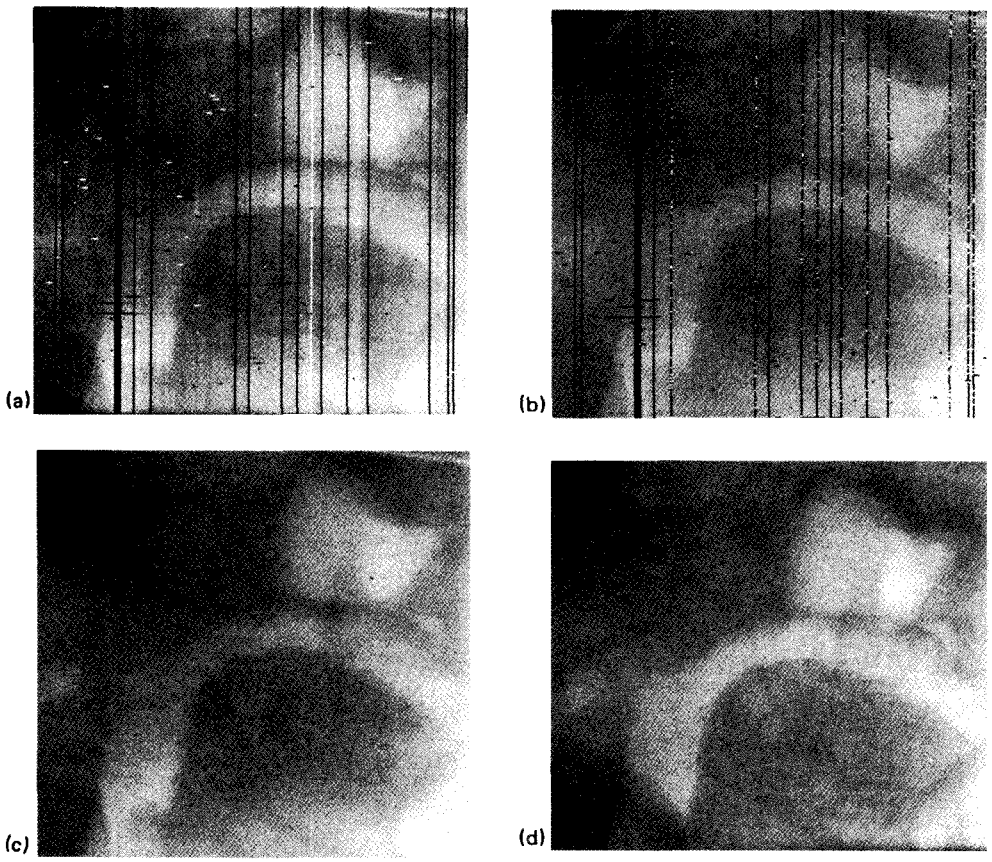

FIG. 9. Megavoltage images of a Rando Alderson head phantom at 6 MV. (a) Image acquired with a 450-μm array taken with 7.5 MUs. The image is the raw data without pixel calibration factors. (b) Image 9(a) after application of calibration constants for the individual pixels. (c) Image 9(b) after application of filters to selected pixels. (d) Digitized film image taken with 5 MUs.

$\sim$1-mm copper sheet and a 0.2-mm-Pb back screen. This dose provided the greatest amount of observable detail for the film image and was just below the saturation level of the film. This and all following film images have been digitized at sampling intervals ranging from 125–200 μm which, in our judgement, enhanced the presentation of their imaging information. Figure 8(c) is an array image acquired at 75 kVp with 7 mA and a 1-s integration period. Figure 8(d) is a digitized film image taken at 74 kVp with a 100 mA, 0.03-s exposure.

Pixel-by-pixel gain and offset corrections have been applied to the array images in Fig. 8(a)(c). Second, a 3×3 median filter has been applied to the 5 bad pixels on the 900-μm array in the same manner as for Fig. 7(c). Finally, a bilinear interpolation has been applied to the 900-μm array images in order to remove the distracting pixelation associated with these relatively small format, coarsely pixelated, images. The images are, in fact, slightly off-lateral due to a slight rotation of the head. In the megavoltage array image of Fig. 8(a), the anterior clinoid process, the sella turcica, the dorsum of sella, the near and far floor of the sphenoid sinus, and the roof of an orbit are visible. This image compares favorably with the corresponding digitized film image of Fig. 8(b). The diagnostic array image of Fig. 8(c) generally exhibits the same information content as the diagnostic film image of Fig. 8(d) although at a far lower resolution due to its comparatively coarse pixel pitch. In both the megavoltage and diagnostic x-ray cases, the array–screen combinations demonstrate roughly the same sensitivity as the film–screen combinations, allowing for the fact that the diagnostic film cassette uses a double screen.

C. Images with 450-μm arrays

Figures 9–11 show megavoltage array and film images of various anthropomorphic phantoms. In all cases, the beam energy was 6 MV, the field was 12×12 cm. The midline of each phantom was at a distance of $\sim$100 cm from the radiation source while the array and film cassette were positioned at 119 cm. The array images were acquired with 7.5 MUs. Array acquisition with fewer MUs was not possible due to constraints imposed by the speed of the readout electronics as well as by the pulse structure of the accelerator.

Figure 9 shows megavoltage array and film images of a Rando Alderson head phantom. Figure 9(a) shows a raw a-Si:H image. The prominent vertical line artifacts correspond to DATA lines which have been disconnected from the external electronics for reasons explained earlier. The other prominent artifact are the short horizontal stripes. These are believed to be due to another form of pixel failure in which the size of the pixel signal during readout is sufficiently large that crosstalk occurs in the preamplifier

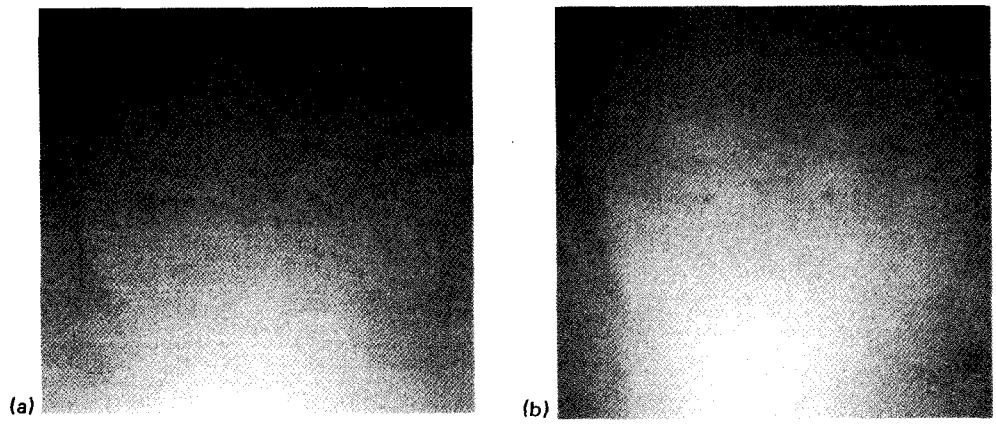

FIG. 10. Megavoltage images of a 3M pelvic phantom at 6 MV. (a) Image acquired with the 450-μm array of Fig. 9 taken with 7.5 MUs. The image processing corresponds to that of Fig. 9(c). (b) Digitized film image taken with 6 MUs.

circuits. Figure 9(b) shows the effect of the application of pixel calibration constants to the unprocessed array image data. Figure 9(c) illustrates the selective application of filters to the image data of Fig. 9(b). First, a 3×3 median filter was applied, as described previously, to pixels whose gain and offset calibration values deviated significantly from the mean. Then, any remaining pixels with a value below an arbitrarily chosen intensity (400) were set to the average value of all the other pixels above this threshold value in a 5×5 pixel region centered on the pixel. The combination of these filters largely, though not completely, removes the distracting influence of the bad pixels and lines. Figure 9(d) is the digitized film image taken with 5 MUs. The general anatomical detail present in the film image, Fig. 9(d), is largely apparent in the array image of Fig. 9(c). This includes the nasopharynx, teeth, and the maxillary sinus.

Figures 10 and 11 show megavoltage array and film images of a 3M pelvic phantom and a chest phantom, respectively. Figures 10(a) and 11(a) show the array images after application of all the image processing steps described for Fig. 9. Figures 10(b) and 11(b) are the digitized films images with 5 MUs. Like the head, both of these anatomical regions represent common radiotherapy treatment sites. However, the chest, and particularly the pelvis, represent more challenging imaging situations as there are relatively fewer high contrast landmarks than in the head. In the pelvis images, the pubic symphysis, ischial tuberosities, obturator foramen, ischium, and other features are visible. In the chest images, pedicles, intervertebral spaces, the aortic arch, and a number of ribs are visible. In addition, two $\sim$2-mm marker BBs were placed on the surface of each phantom and four $\sim$1.3-mm BBs were placed on the pelvis phantom. These smaller BBs are placed in the prostate under transrectal ultrasound guidance as part of a current protocol at our institution.[31] All of these BBs stand out well in both the array and film images.

Figures 12 and 13 show diagnostic x-ray array and film images of a larger region of the foot and head phantoms imaged in Figs. 7 and 8, respectively. For the head image of Fig. 13, the 450-μm array used was a different one from that used for the other diagnostic and megavoltage images. (The images shown in Figs. 9–12 were first presented on 23 February, 1992 at the SPIE Medical Imaging VI meeting held in Newport Beach, CA, 23–27 February, 1992. A foot image similar to that of Fig. 12 was first presented at the

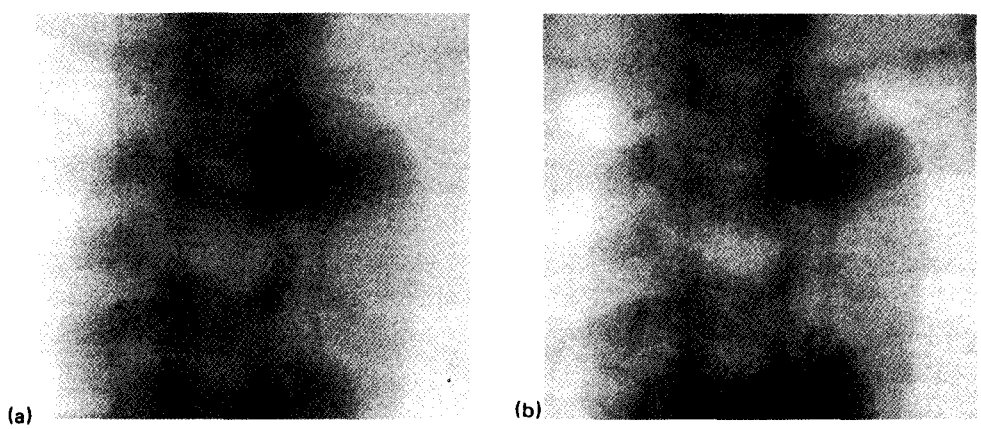

FIG. 11. Megavoltage images of a chest phantom at 6 MV. (a) Image acquired with the 450-μm array of Fig. 9 taken with 7.5 MUs. The image processing corresponds to that of Fig. 9(c). (b) Digitized film image taken with 6 MUs.

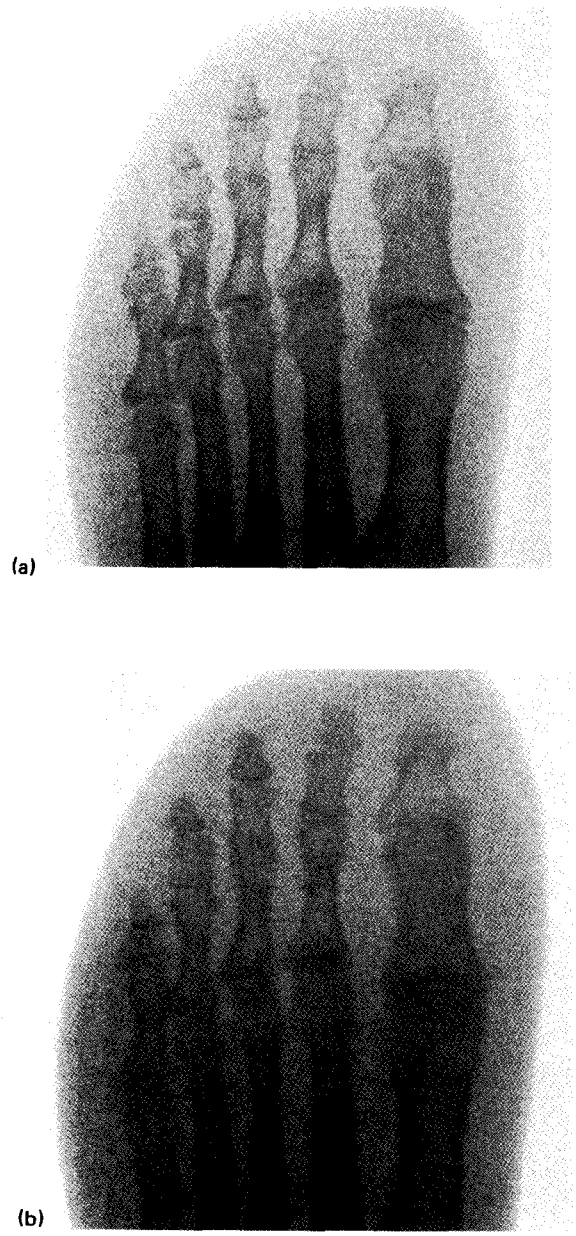

FIG. 12. Diagnostic x-ray images of a foot phantom at 65 kVp. (a) Image acquired with the 450-μm array of Fig. 9 taken with 0.75-mAs exposure. The image processing corresponds to that of Fig. 9(c). (b) Digitized film image taken with 0.35-mAs exposure.

1991 ASTRO Annual Meeting.) The midline of each phantom was at a distance of 100 cm from the radiation source while the array and film cassette were at 104 and 114 cm for the foot and head phantoms, respectively. The field size was approximately 30×30 cm at the midline of the phantoms. For the foot phantom, the array image was acquired at 65 kVp with a 50 mA, 0.015-s exposure while the film image was also acquired at 65 kVp but with a 50 mA, 0.007-s exposure. For the head phantom, the array image was acquired at 75 kVp with a 3.5 mA, 2-s exposure while the film image was acquired at 74 kVp with a 100 mA, 0.03-s exposure. Figures 12(a) and 13(a) show the array images after application of all the image processing steps described for Fig. 9. Figures 12(b) and 13(b) are the digitized film images.

The array foot image in Fig. 12 shows a clear definition of the joint spaces. In particular, the metatarsal-phalangeal joints are well defined. Moreover, one can appreciate the trabecular structure of the heads of the metatarsals. In Fig. 13, the head rotation and BB positions are different from that of Fig. 8. Due to a greater concentration of bad pixels near the disabled DATA lines for this array, the filtering for Fig. 13(a) is less successful in removing distracting artifacts than for Fig. 12(a). Nevertheless, considerable detail can be discerned from the array head image of Fig. 13(a) including the maxillary ridge, the mastoid regions, the nonoverlapping mandibular condyles, the sella turcica, the dorsum sellae, the sphenoid sinus, and the floor and roof of the orbit.

V. DISCUSSION AND CONCLUSIONS

A new form of flat-panel imaging technology for diagnostic x-ray and megavoltage imaging is under development by our collaboration and has been described in this article. The arrays, the general form of the external electronics required to operate them, and their operation have been presented. The details of the means and techniques required to produce diagnostic x-ray and megavoltage images have been given, and a variety of low and high contrast images have been presented. The first megavoltage images and the first diagnostic images of an anatomical

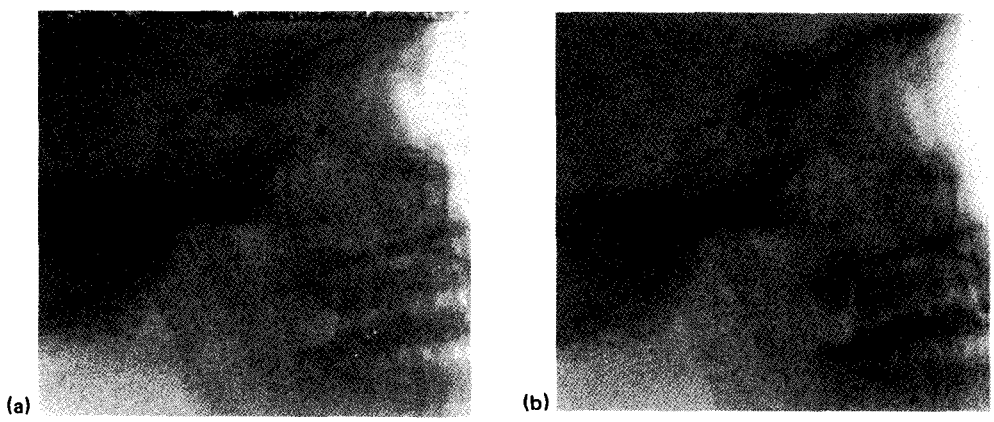

FIG. 13. Diagnostic x-ray images of a head phantom. (a) Image acquired with a 450-μm array taken at 75 kVp with 7.0-mAs exposure. The image processing corresponds to that of Fig. 9(c). (b) Digitized film image taken at 74 kVp with 3.0-mAs exposure.

phantom using such a-Si:H imaging arrays have been presented. Overall, the megavoltage array images compare favorably with the corresponding digitized film images. In addition, the diagnostic x-ray array images generally present contrast information similar to that of the corresponding digitized film images although at a lower spatial resolution. Beyond this initial imaging demonstration, a more quantitative examination of the dynamic range and resolution capabilities of these arrays using standard contrast and detail phantoms would assist in evaluating their overall imaging performance. Anticipated improvements in the quality of the arrays, of the readout electronics, and in the calibration and operating procedures should allow such an examination in the near future.

Thus far, our experience in developing this new form of imager leads to several interesting observations. First, while the design and fabrication of the arrays themselves has proceeded faster than planned, it has proven to be an extremely sound strategy to continually try out new ideas for array improvement on the small format (64×40) arrays while cautiously proceeding with the development of larger format arrays. This is true simply because the smaller arrays are easier to mount, handle, develop electronics for, and require fewer resources to alter and fabricate. Second, while progress has been substantial since the commencement of this project several years ago, there remain a number of important details to be explored. One question concerns the degree to which current leaking through the FETs during integration could result in a partial loss of imaging information. Another is the degree to which the capture and release of charge in deep trapping states in the sensors might contribute to image lag. Yet another question is the extent to which long term drifts in the sensor leakage currents may affect calibration procedures. These matters are currently under investigation.

Finally, several "peripheral" nonarray issues have proven to be major challenges. One example is the lack of an inexpensive, standardized, robust, and reliable connection technology for attaching the arrays to external circuit boards in a convenient fashion. This problem currently has no completely satisfactory solution, and our needs are presently being met either by wire bonding or elastomeric connector techniques. Another example is the fact that the electronics development has turned out to be at least as large a challenge as the arrays themselves. The large number of independent DATA lines provide relatively small analog signals at high rates. The ultimate clinical implementation of this imaging technology will require sophisticated analog and digital control logic as well as the development of multichannel (16 to 64) charge-sensitive preamplifier-multiplexer integrated circuits whose signal characteristics are closely matched to the signal and noise characteristics of the arrays and the particular imaging application. The development of such integrated circuits, already begun in the particle physics community, is technically feasible and the required monolithic electronic circuits should eventually become available.

In conclusion, we are extremely encouraged by the promise thus far shown by this new imaging technology. Clinical implementation of such flat panel imagers could have a profound impact given their anticipated advantages. Besides the aforementioned advantages over XRIIs currently used in diagnostic fluoroscopy and camera-fluoroscopy systems used in megavoltage imaging, the intriguing possibility of a film substitute exists. However, the current state of the technology limits the minimum pixel sizes to $\sim100\ \mu m$ and prevents the incorporation of the external electronics into the arrays themselves. Thus further progress in the underlying thin-film electronics technology will probably be necessary before very high resolution film substitutes are a reality. Fortunately, current world-wide interest in developing progressively more elaborate flat-panel displays will mean that the large costs associated with developing the base technology of thin-film electronics and the fabrication facilities for arrays, which could never be assumed by the relatively smaller medical imaging industry, will be borne by the display industry. Thus we anticipate that the complexity and power of these arrays will increase and their ultimate cost will be low. However, a sustained research effort will be required to develop both the arrays and associated electronics to allow comprehensive study of the imaging properties and clinical value of these imagers. The 1990s should see some extremely interesting developments in this regard.

ACKNOWLEDGMENTS

We would like to thank Mr. Parag Mody, Mr. James Berry, and Mr. Helmut Schick for their contributions to the creation of the electronic readout system, Kathy Lash, for her assistance in the creation of the foam support for the head phantom, and Ms. Mary Kay Witkowski for her assistance in the creation of the film images. We would like to express our appreciation to Richard Weisfield of Xerox, PARC for providing the sensor light efficiency data of Fig. 3. Finally, we would like to thank Kwok Lam, for his assistance with the film digitizer, Loren T. Niklason, for assistance with the phantoms, and Heang-Ping Chan, Benedick A. Fraass, Mary Victoria Marx, and Howard M. Sandler, for valuable discussions. This work is supported by the National Institutes of Health, Grant No. 1-R01-CA51397-03.

[1]M. P. Capp, "Radiological imaging-2000 A.D.," Radiology **138**, 541–550 (1981).

[2]S. Nudelman, H. Roehrig, and M. P. Capp, "A study of photoelectronic-digital radiology-part III: image acquisition components and system design," Proc. IEEE **70**(7), 715–727 (1982).

[3]A. Rose and P. K. Weimer, "Physical limits to the performance of imaging systems," Physics Today **42**(9), 24–32 (1989).

[4]For information concerning the physics and technology of hydrogenated amorphous silicon, useful references are: J. D. Joannopoulos and G. Lucovsky, eds., *The Physics of Hydrogenated Amorphous Silicon I*, Topics in Appl. Phys. **55** (Springer-Verlag, Berlin, 1984). J. D. Joannopoulos and G. Lucovsky, eds., *The Physics of Hydrogenated Amorphous Silicon II*, Topics in Appl. Phys. **56** (Springer-Verlag, Berlin, 1984). R. A. Street, *Hydrogenated Amorphous Silicon* (Cambridge U.P., MA, 1991).

[5]V. Perez-Mendez, S. N. Kaplan, W. Ward, S. Qureshi, and R. A. Street, "Signal, recombination effects and noise in amorphous silicon detectors," Nucl. Instr. Meth. **A260**, 195–200 (1987).

[6]L. E. Tannas Jr., "Flat-panel displays displace large, heavy, power-hungry CRTs," IEEE Spectrum **26**(9), 34–35 (September 1989).

[7]J. A. Adam, "Industries transcend national boundaries," IEEE Spectrum **27**(9), 26–31 (1990).
[8]V. Perez-Mendez, G. Cho, J. Drewrey, I. Fujieda, S. N. Kaplan, S. Qureshi, and R. A. Street, in *Physics and Applications of Amorphous and Microcrystalline Semiconductor Devices*, edited by J. Kanicki (Artech House, Boston, 1991), Chap. 8.
[9]T. Takahashi, H. Itoh, T. Shimada, and H. Takeuchi, "Design of integrated radiation detectors with a-Si:H photodiodes on ceramic scintillators for use in x-ray computed tomography," IEEE Trans. Nucl. Sci. **37**(3), 1478–1482 (1990).
[10]Y. Naruse and T. Hatayama, "Metal/amorphous silicon multilayer radiation detectors," IEEE Trans. Nucl. Sci. **36**, 1347–1352 (1989).
[11]K. Hasegawa, K. Mochiki, H. Takahashi, S. Namatame, and Y. Satow, "Imaging system with an amorphous silicon linear sensor," Rev. Sci. Instrum. **60**(7), 2284–2286 (1989).
[12]L. E. Antonuk, J. Yorkston, J. Boudry, M. J. Longo, J. Jimenez, and R. A. Street, "Development of hydrogenated amorphous silicon sensors for high energy photon radiotherapy imaging," IEEE Trans. Nucl. Sci. **37**(2), 165–170 (1990).
[13]L. E. Antonuk, C. W. Kim, J. Boudry, J. Yorkston, M. J. Longo, and R. A. Street, "Development of hydrogenated amorphous silicon sensors for diagnostic x-ray imaging," IEEE Trans. Nucl. Sci. **38**(2), 636–640 (1991).
[14]L. E. Antonuk, J. Yorkston, J. Boudry, M. J. Longo, and R. A. Street, "Large area amorphous silicon photodiode arrays for radiotherapy and diagnostic imaging," Nucl. Instr. Meth. **A310**, 460–464 (1991).
[15]L. E. Antonuk, J. Boudry, C. W. Kim, M. Longo, E. J. Morton, J. Yorkston, and R. A. Street, "Signal, noise, and readout considerations in the development of amorphous silicon photodiode arrays for radiotherapy and diagnostic x-ray imaging," SPIE **1443**, Medical Imaging V: Imaging Physics 108–119 (1991).
[16]P. Munro, J. A. Rawlinson, and A. Fenster, "Therapy imaging: A signal-to-noise analysis of a fluoroscopic imaging system for radiotherapy localization," Med. Phys. **17**(5), 763 (1990).
[17]P. Munro, J. A. Rawlinson, and A. Fenster, "A digital fluoroscopic imaging device for radiotherapy localization," Int. J. Radiation Oncology Biol. Phys. **18**, 641–649 (1990).
[18]E. J. Morton, W. Swindell, D. G. Lewis, and P. M. Evans, "A linear array, scintillation crystal-photodiode detector for megavoltage imaging," Med. Phys. **18**, 681–691 (1991).
[19]J. Yorkston, L. E. Antonuk, E. J. Morton, J. Boudry, W. Huang, C. W. Kim, M. J. Longo, and R. A. Street, "The dynamic response of hydrogenated amorphous silicon imaging pixels," Mat. Res. Soc. Symp. Proc. **219**, 173–178 (1991).
[20]R. A. Street, S. Nelson, L. E. Antonuk, and V. Perez Mendez, "Amorphous silicon sensor arrays for radiation imaging," Mat. Res. Soc. Proc. **192**, 441–452 (1990).
[21]L. E. Antonuk, J. Yorkston, C. W. Kim, W. Huang, E. J. Morton, M. J. Longo, and R. A. Street, "Light-response characteristics of amorphous silicon arrays for megavoltage and diagnostic imaging," Mat. Res. Soc. Symp. Proc. **219**, 531–536 (1991).
[22]L. E. Antonuk, J. Yorkston, W. Huang, J. Boudry, E. J. Morton, M. J. Longo, and R. A. Street, "Radiation response characteristics of amorphous silicon arrays for megavoltage radiotherapy imaging," IEEE Trans. Nucl. Sci. **39**(4), 1069–1073 (1992).
[23]L. E. Antonuk, J. Boudry, J. Yorkston, C. F. Wild, M. J. Longo, and R. A. Street, "Radiation damage studies of amorphous silicon photodiode sensors for applications in radiotherapy x-ray imaging," Nucl. Instru. Meth. **A299**, 143–146 (1990).
[24]H. Itoh, S. Matsubara, T. Takahashi, T. Shimada, and H. Takeuchi, "Integrated radiation detectors with a-Si photodiodes on ceramic scintillators," Jap. J. App. Phys. **28**(8), L1476–L1479 (1989).
[25]I. D. French, A. J. Snell, P. G. LeComber, and J. H. Stephen, "The effect of gamma-irradiation on amorphous silicon field effect transistors," Appl. Phys. **A31**, 19–22 (1983).
[26]P. Munro, J. A. Rawlinson, and A. Fenster, "A digital fluoroscopic imaging system for radiotherapy localization," Proc. SPIE **1090**, 321–329 (1989).
[27]I. Fujieda, S. Nelson, R. A. Street, and R. L. Weisfield, "Radiation imaging with 2D a-Si sensor arrays," IEEE Trans. Nucl. Sci. **39**(4), 1056–1062 (1992).
[28]J. Lewis, G. M. McPherson, M. C. Morrissey, J. C. Thompson, and A. W. Tucker, "A monolithic charge multiplexer with 0.5% accuracy," Nucl. Instr. Meth. **A288**, 197–208 (1990).
[29]R. C. Ball, H. R. Gustafson, M. J. Longo, and T. J. Roberts, "An inexpensive, high performance pulse-height readout system for proportional chambers," Nucl. Instr. Meth. **197**, 371–377 (1982).
[30]B. G. Taylor, "Macintosh in the laboratory," CERN technical note CERN-EP/88-67 (1988).
[31]H. M. Sandler, R. L. Bree, P. W. McLaughlin, H. B. Grossman, and A. S. Lichter, "Localization of the prostate apex for radiotherapy using implantable markers," 1992 ASTRO abstract.